AAAS
Research
Volume 2020, Article ID 2360796, 9 pages
https://doi.org/10.34133/2020/2360796

Research
A SCIENCE PARTNER JOURNAL

Research Article

Stereoassembled V_2O_5@FeOOH Hollow Architectures with Lithiation Volumetric Strain Self-Reconstruction for Lithium-Ion Storage

Yao Zhang,[1] Kun Rui,[1] Aoming Huang,[1] Ying Ding,[1] Kang Hu,[1] Wenhui Shi,[2] Xiehong Cao,[3] Huijuan Lin,[1] Jixin Zhu,[1] and Wei Huang[1,4]

[1]*Key Laboratory of Flexible Electronics (KLOFE) & Institute of Advanced Materials (IAM), Nanjing Tech University (NanjingTech), 30 South Puzhu Road, Nanjing 211816, China*
[2]*Center for Membrane and Water Science & Technology, Ocean College, Zhejiang University of Technology, Hangzhou 310014, China*
[3]*College of Materials Science and Engineering, Zhejiang University of Technology, 18 Chaowang Road, Hangzhou, Zhejiang 310014, China*
[4]*Shaanxi Institute of Flexible Electronics (SIFE), Northwestern Polytechnical University (NPU), 127 West Youyi Road, Xi'an 710072, China*

Correspondence should be addressed to Kun Rui; iamkrui@njtech.edu.cn and Jixin Zhu; iamjxzhu@njtech.edu.cn

Received 29 January 2020; Accepted 12 March 2020; Published 8 April 2020

Vanadium oxides have recently attracted widespread attention due to their unique advantages and have demonstrated promising chemical and physical properties for energy storage. This work develops a mild and efficient method to stereoassemble hollow V_2O_5@FeOOH heterostructured nanoflowers with thin nanosheets. These dual-phased architectures possess multiple lithiation voltage plateau and well-defined heterointerfaces facilitating efficient charge transfer, mass diffusion, and self-reconstruction with volumetric strain. As a proof of concept, the resulting V_2O_5@FeOOH hollow nanoflowers as an anode material for lithium-ion batteries (LIBs) realize high-specific capacities, long lifespans, and superior rate capabilities, e.g., maintaining a specific capacity as high as 985 mAh g^{-1} at 200 mA g^{-1} with good cyclability.

1. Introduction

Featuring high theoretical lithium storage capacity, considerable structural versatility and appealing electrochemical reactivity, transition metal oxides (TMOs, e.g., M_xO_y, M=Cu, Fe, Co, Ni, Mn, etc.) have received tremendous interest for potential energy storage applications [1–5]. Moreover, TMOs are endowed with enhanced safety as anode materials for lithium-ion batteries (LIBs), as the lithium dendrite growth can be inhibited at a relatively higher lithiation reaction potential. Therefore, TMOs have been widely explored and designed with expected structures, compositions, and size [6–9]. Particularly, vanadium oxides can intercalate more lithium ions owing to the distinct feature of multiple oxidation states (V^{2+} to V^{5+}) [10–14]. In practice, despite the high theoretic capacity as both anode and cathode materials for LIBs, low electrical conductivity and large volumetric strains of V_2O_5 inevitably render poor rate capability and cycling stability [15–17]. To address these issues, carbon modification has been one of the most intuitive approaches to promote the electron transport for numerous TMOs-based electrode materials [18–20].

Alternatively, developing well-defined structures has also demonstrated great promise for boosting the electrochemical properties including enhanced capacity as well as desired stability [21–24]. For example, hierarchical assemblies consisting of nanosized building blocks, i.e., one-dimensional (1D) or two-dimensional (2D) subunits, are provided with combined merits of further enlarged contact area with electrolyte and reduced charge/mass diffusion pathways [25–28]. However, sacrificial templates associated with multistep procedures are usually involved for carefully designed complex

structures. Furthermore, heterostructures through coupling versatile species are believed to offer more opportunities for various areas, which results from regulated electronic structures and intriguing synergistic effect at well-defined heterointerfaces [29–33]. More importantly, rational integration of functional components with consideration of their intrinsic redox properties allows tailored electrochemical behaviors for energy-based applications [34, 35]. To date, efficient construction of heterostructured electrodes based on V_2O_5 with tunable complex nanostructures remains a big challenge.

Herein, we demonstrate an efficient and facile method to stereoassemble dual-phased architectures of V_2O_5@FeOOH under a mild condition. Hierarchical V_2O_5@FeOOH heterostructures with well-defined morphology and composition are composed of highly connected ultrathin nanosheets, featuring well-defined heterointerfaces and multiple lithiation voltage plateau. Specifically, the V_2O_5@FeOOH with hollow nanoflower structures are well presented, enabling efficient charge transfer, mass diffusion, and self-reconstruction with volumetric strain. As a proof-of-concept demonstration, the V_2O_5@FeOOH hollow nanoflower anode delivers boosted Li-storage properties including high-specific capacities, long lifespans, and superior rate capabilities. Remarkably, a high-specific capacity of 985 mAh g^{-1} at 200 mA g^{-1} is achieved with good cyclability.

2. Results and Discussion

The facile synthetic procedure of dual-phased hollow architectures is illustrated in Figure 1. The stereoassembled V_2O_5@FeOOH hollow heterostructures are obtained by using commercial V_2O_5 as the starting material under a mild condition (see the Experimental section for details). Specifically, irregular bulk V_2O_5 powders (Figure S1) are first dispersed in deionized water, followed by dropwise addition of hydrogen peroxide (H_2O_2) at room temperature to form a uniform solution. During which, the dissolution of V_2O_5 with the presence of H_2O_2 results in the formation of complex vanadium-based intermediates [36]. Afterward, the self-assembly of V_2O_5 nanosheets into well-defined hierarchical hollow architecture can be realized with the assistance of iron(III) nitrate nonahydrate ($Fe(NO_3)_3{\cdot}9H_2O$) at 50°C by controlling the reaction time (Figures S2-S6). Importantly, $Fe(NO_3)_3$ in this case acts as the shape-directing agent to manipulate the morphology, as bare 2D nanosheets with large lateral size and smooth surface can be obtained without the addition of $Fe(NO_3)_3$ (Figure S7). Furthermore, $Fe(NO_3)_3$ contributes to the nanoscale heterostructuring with optimized composition through in situ deposition of FeOOH as well. Lastly, a reddish-brown V_2O_5@FeOOH product can be harvested after a vacuum freeze-drying process.

The morphology and structure of the V_2O_5@FeOOH heterostructures are investigated by field emission scanning electron microscopy (FESEM). As presented by the panoramic image in Figure 2(a), these V_2O_5@FeOOH particles exhibit a flower-like sphere structure with high uniformity. A closer FESEM examination revealed the hierarchical architecture of V_2O_5@FeOOH, which are assembled from nanosheet subunits with a small thickness of about 10 nm (Figure 2(b)). Interestingly, a well-defined hollow interior of approximately 300 nm can be clearly observed from the transmission electron microscopy (TEM) image (Figure 2(c)). At a higher magnification, the thin character of these wrinkled nanosheets is suggested by their high transparency under the electron beam (Figure 2(d)). Notably, a set of diffraction spots well fit the orthorhombic V_2O_5 lattice structure, which is viewed along the [010] zone axis according to the selected area electron diffraction (SAED) data (Figure S8). In the high-resolution TEM (HRTEM) image (Figure 2(e)), the crystalline nanosheet shows typical lattice spacings of 0.23 nm and 0.20 nm, corresponding to the (113) and (006) planes of $V_2O_5{\cdot}1.6H_2O$. Meanwhile, notably discontinuous lattice fringes can be observed, which can be readily attributed to the vertical coverage of amorphous FeOOH domains. Moreover, scanning transmission electron microscopy-energy dispersive spectroscopy (STEM-EDS) elemental mapping images of V_2O_5@FeOOH corresponding to the dark-field image (Figure 2(g)) reveal the homogeneous distribution of V, Fe, and O (Figure 2(h)). As demonstrated by the EDS line scan profile in Figure 2(f), both V and Fe signals exhibit relatively higher intensity at the edge region as compared to the core region, further validating the formation of hollow structure.

It is worth noting that the configuration of V_2O_5@FeOOH heterostructure can be precisely tuned by varying the amount of Fe(III) precursor (Figure 3). Interestingly, the flower-like V_2O_5@FeOOH spheres expanded significantly with the increasing amount of Fe(III) precursor. In sharp contrast to V_2O_5@FeOOH-1 that is obtained by using $Fe(NO_3)_3$ and V_2O_5 with a mass ratio of 1 : 1 (Figures 3(a) and 3(b)), V_2O_5@FeOOH-2 evolves into irregular assembly of nanosheets, exhibiting open cavities as surrounding 2D building blocks tend to spread out (Figures 3(c) and 3(d)). Importantly, the hierarchical hollow structure hardly maintains when further increasing the mass ratio of $Fe(NO_3)_3$ to V_2O_5 (V_2O_5@FeOOH-5). Highly interconnected 3D architectures can be obtained, which are constructed from randomly assembled nanosheets with rough surfaces (Figures 3(e) and 3(f)). For comparison, bare FeOOH particles can be obtained by the same procedure except for the presence of V_2O_5 (Figure S9).

The crystal structure of as-synthesized samples is then determined through X-ray diffraction (XRD) measurement (Figure 4(a)). For V_2O_5@FeOOH-1, the diffraction peaks at 8.3°, 25.9°, 31.1°, 34.2°, 46.4°, and 50.3° can be well assigned to (001), (101), (004), (103), (006), and (200) reflections of orthorhombic structured $V_2O_5{\cdot}1.6H_2O$ (JCPDS no. 40-1296). On the other hand, no characteristic peaks belonging to FeOOH are detected, which should be attributed to its amorphous feature [37]. The lower crystallinity of V_2O_5@FeOOH-2 and V_2O_5@FeOOH-5 as indicated by the disappearing of well-defined diffraction peaks further suggest the increased content of amorphous phase within the V_2O_5@FeOOH hybrids. The chemical composition and bonding state of V_2O_5@FeOOH are also investigated by X-ray photoelectron spectroscopy (XPS). The high-resolution

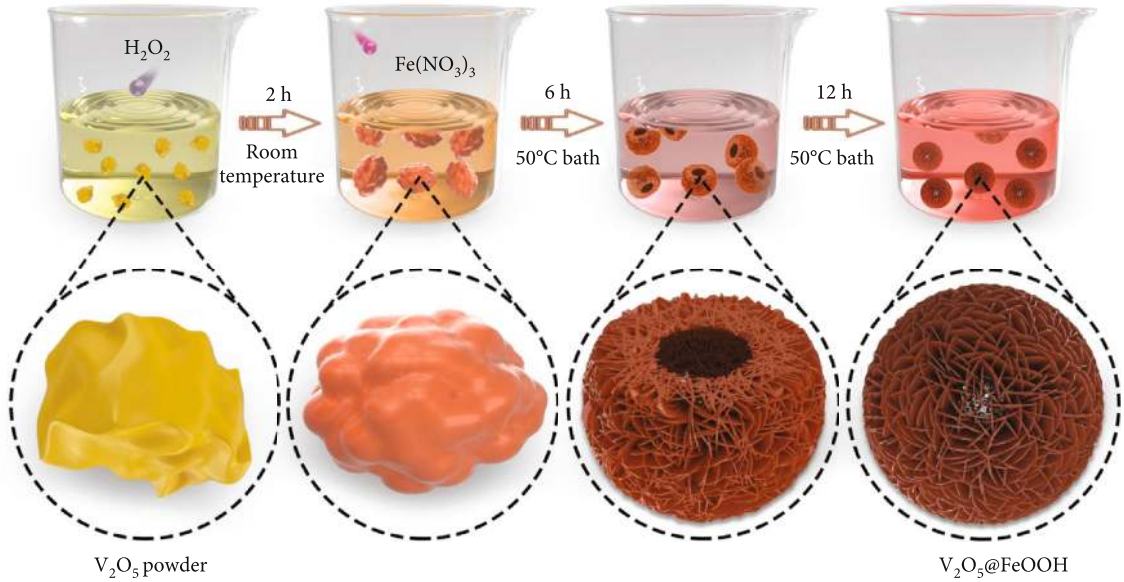

Figure 1: Schematic illustration for the stereoassembled V_2O_5@FeOOH hollow heterostructure.

Fe 2p spectra (Figure 4(b) and Figure S10) confirm the presence of Fe species as FeOOH [38, 39], with the coexistence of Fe^{2+} and Fe^{3+} at 710.7/724.8 eV and 712.8/727.8 eV, respectively. The peak intensity for Fe $2p_{1/2}$, $2p_{3/2}$, and satellite together enlarged from V_2O_5@FeOOH-1 to V_2O_5@FeOOH-5, in accordance with the increasing incorporation of Fe species within the heterostructure (Table S1). The V 2p region spectra of V_2O_5@FeOOH are analyzed, exhibiting characteristic peaks centered at 524.6 and 517.0 eV for V^{5+} components of V_2O_5 (Figure 4(c)) [40–42]. Besides, a negative shift of binding energy (~0.8 eV) for both V $2p_{1/2}$ and $2p_{3/2}$ bands are achieved as compared to bare V_2O_5 (Figure S11), indicating the strong electronic interaction at the V_2O_5/FeOOH interfaces. Meanwhile, the deconvoluted O 1s core level spectra show two dominant peaks that can be assigned to V-O and Fe-O-Fe bonds [43], which reveal varied portions of the Fe-O-Fe at 530.4 eV accordingly (Figure 4(d)).

As a proof of concept, the electrochemical properties of heterostructured V_2O_5@FeOOH as LIB anodes are examined (Figure 5). The initial Coulombic efficiency (CE) is around 50% for V_2O_5@FeOOH (e.g., 50% for V_2O_5@FeOOH-1, 53% for V_2O_5@FeOOH-2, and 43% for V_2O_5@FeOOH-5), which can be attributed to the irreversible capacity loss due to the formation of solid electrolyte interphase (SEI) film on the electrode surface [44]. After a typical activation process for 50 cycles [45], remarkable reversible capacities as high as 985, 1016, and 1030 mAh g^{-1} at a current density of 200 mA g^{-1} are delivered by V_2O_5@FeOOH-1, V_2O_5@FeOOH-2, and V_2O_5@FeOOH-5, respectively, reaching the CE of nearly 100%. The desirable Li-storage capacities surpassing bare V_2O_5 (635 mAh g^{-1}) and FeOOH (342 mAh g^{-1}) manifest the superiority of dual-phased heterostructures constructed by 2D building blocks. Different from V_2O_5@FeOOH-2 and V_2O_5@FeOOH-5 with capacity fading after ca. 100 cycles, 96% capacity is retained for V_2O_5@FeOOH-1 after 180 cycles, which can be further attributed to its well-defined hollow configuration. The 3D hierarchical structure integrity of V_2O_5@FeOOH-1 can be maintained during repeated Li^+ insertion and exaction as confirmed by postmortem FESEM images in Figure S12. Of note, the cycling stability of V_2O_5@FeOOH-1 can be further highlighted at a higher current density of 2000 mA g^{-1}, i.e., 494 mAh g^{-1} after 300 cycles with a high capacity retention of 95% (Figure S13).

Importantly, rate performance of the V_2O_5@FeOOH-1 anode was investigated at different current densities from 100 mA g^{-1} to 3000 mA g^{-1} (Figure 5(b)). Reversible capacities of 992, 947, 906, 856, 714, 519, and 366 mAh g^{-1} are achieved at current densities of 100, 200, 300, 500, 1000, 2000, and 3000 mA g^{-1}, respectively. Cyclic voltammetry (CV) profiles at different scan rates from 0.2 to 1.0 mV s^{-1} were therefore recorded to verify the electrochemical kinetics of V_2O_5@FeOOH-1 for Li-storage (Figure 5(c)). Negligible peak shifts are observed as the scan rates increase, suggesting small polarization as well as desirable kinetics of V_2O_5@FeOOH-1 at high rates. The relationship of log (i, peak current) versus log (v, scan rate) was plotted to give the fitted values of slope b (Figure S14), which provides insights into the charge storage mechanism according to the power-law formula $i = av^b$ [46]. Specifically, a b value of 0.5 represents an ideal diffusion-controlled process, whereas 1.0 indicates a surface capacitive-controlled one. The calculated b values are 0.74 for anodic peak 1 and 0.83 and 0.72 for the cathodic peaks 2 and 3, respectively, demonstrating a partial capacitive-controlled behavior of V_2O_5@FeOOH-1. Quantitative analysis further reveals that the ratios of capacitive contribution gradually improve upon increasing the scan rates (Figure 5(d), see calculation details and Figure S15 in Supplementary Materials), which reaches 67.16% at 1.0 mV s^{-1} (Figure S16). The considerable pseudocapacitive contributions can be readily attributed to the presence of abundant amorphous domains and numerous grain boundaries on the surface of highly

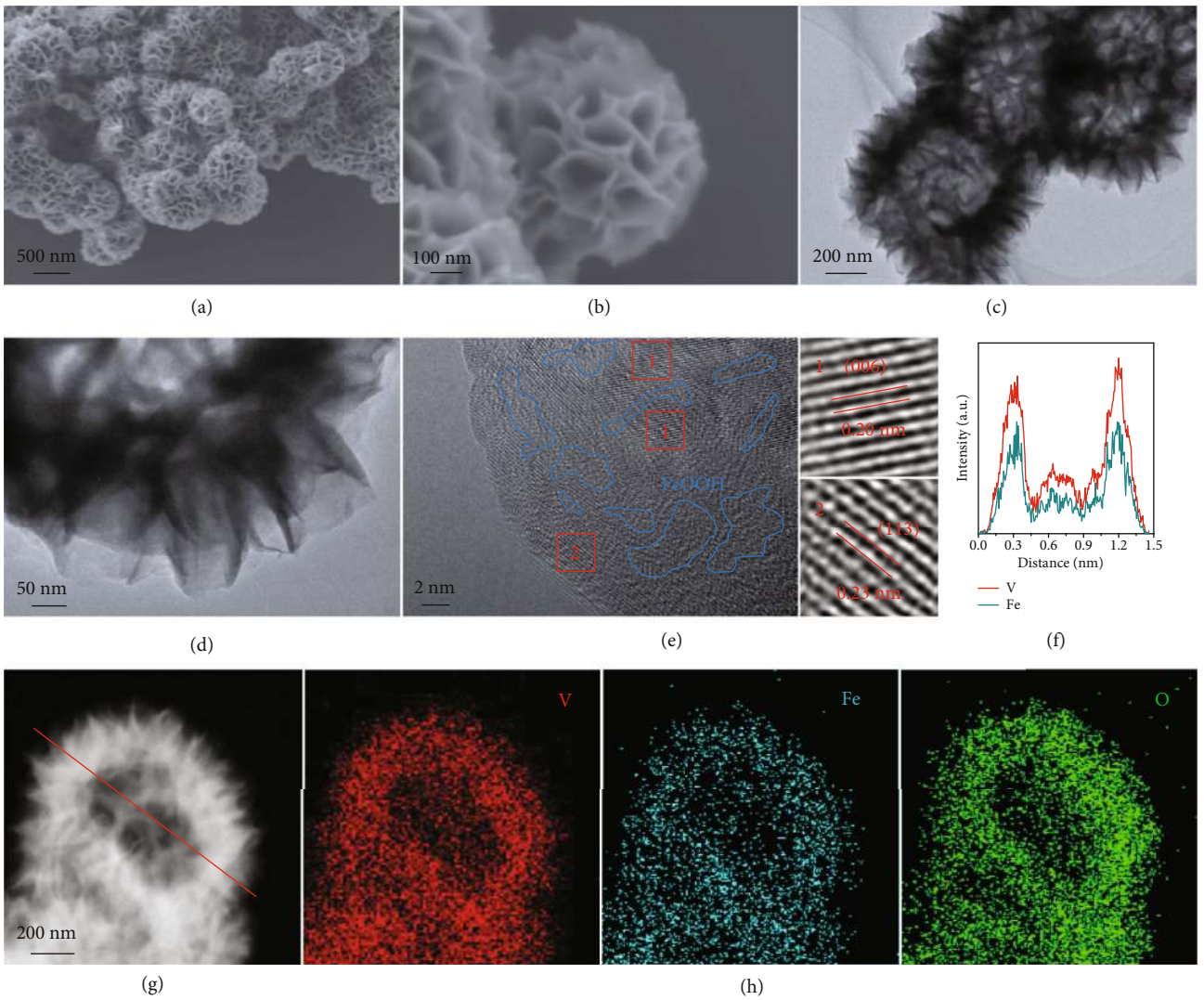

FIGURE 2: Microstructure characterization and composition analysis of hollow V_2O_5@FeOOH heterostructure. (a, b) FESEM images of V_2O_5@FeOOH. (c, d) TEM images of V_2O_5@FeOOH. (e) HRTEM image of V_2O_5@FeOOH. (f) Dark-field STEM-EDS line scan profile of V_2O_5@FeOOH. (g, h) Dark-field TEM image and corresponding elemental mapping images of V_2O_5@FeOOH with red for V, cyan for Fe, and green for O.

exposed nanosheets. These electrochemically active sites are undoubtedly favorable for boosting Li-storage capacity and especially rate performance of V_2O_5@FeOOH-1 hybrid. Furthermore, Nyquist plots demonstrated reduced charge transfer resistances (R_{ct}) of V_2O_5@FeOOH-1 (114.7 Ω) as compared to FeOOH (125.5 Ω), and $V_2O_5{\cdot}nH_2O$ (181.0 Ω), which was fitted according to the equivalent circuit (Figure S17 and Table S2). Moreover, the plot slope of Z' vs. $\omega^{-1/2}$ can be obtained to illustrate the speed of lithium diffusion, which is calculated to be 83.7 for V_2O_5@FeOOH-1, 171.3 for FeOOH, and 128.2 for $V_2O_5{\cdot}nH_2O$ (Figure S18). Therefore, the lithium diffusion coefficients at 25°C are calculated to be 5.98×10^{-14}, 5.28×10^{-15}, and 2.55×10^{-14} c $m^2\ s^{-1}$ for V_2O_5@FeOOH-1, FeOOH, and $V_2O_5{\cdot}nH_2O$, respectively. The results indicate that the V_2O_5@FeOOH-1 hybrid can provide more accessible pathway for charge transfer due to the sufficient heterointerface and accelerated lithium diffusion, resulting in enhanced Li-storage performance.

Additionally, Li-storage performance of V_2O_5@FeOOH-1 are superior to that of many other reported vanadium-based oxide materials (Table S3). The substantially optimized electrochemical properties can be ascribed to the rational construction of V_2O_5@FeOOH heterostructures with well-defined 3D configurations featuring intriguing interfaces and synergistic effects. Specifically, the V_2O_5 nanosheets in the first place serve as ideal building blocks with promoted Li^+/electron transport owing to their ultrathin feature. After introducing amorphous FeOOH, the Li intercalation process can be readily tailored due to the distinct lithiation voltage plateau of FeOOH and V_2O_5 as schematically illustrated in Figure 5(e). Upon discharge, the lithiation of V_2O_5 occurs at

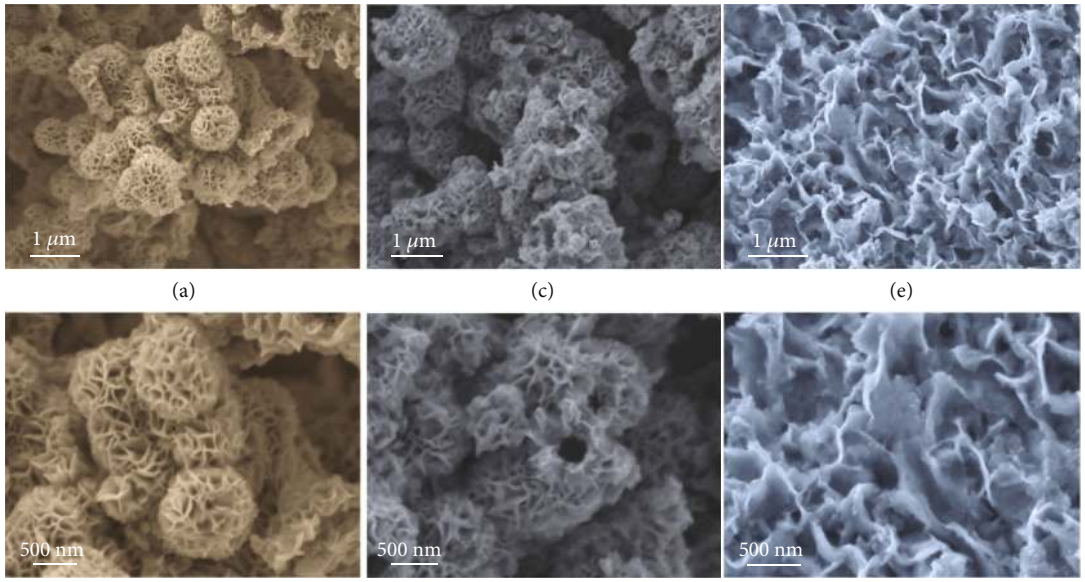

Figure 3: FESEM images of V_2O_5@FeOOH heterostructures obtained by altering the mass ratio of Fe(III) precursor and V_2O_5. (a, b) V_2O_5@FeOOH-1, (c, d) V_2O_5@FeOOH-2, and (e, f) V_2O_5@FeOOH-5.

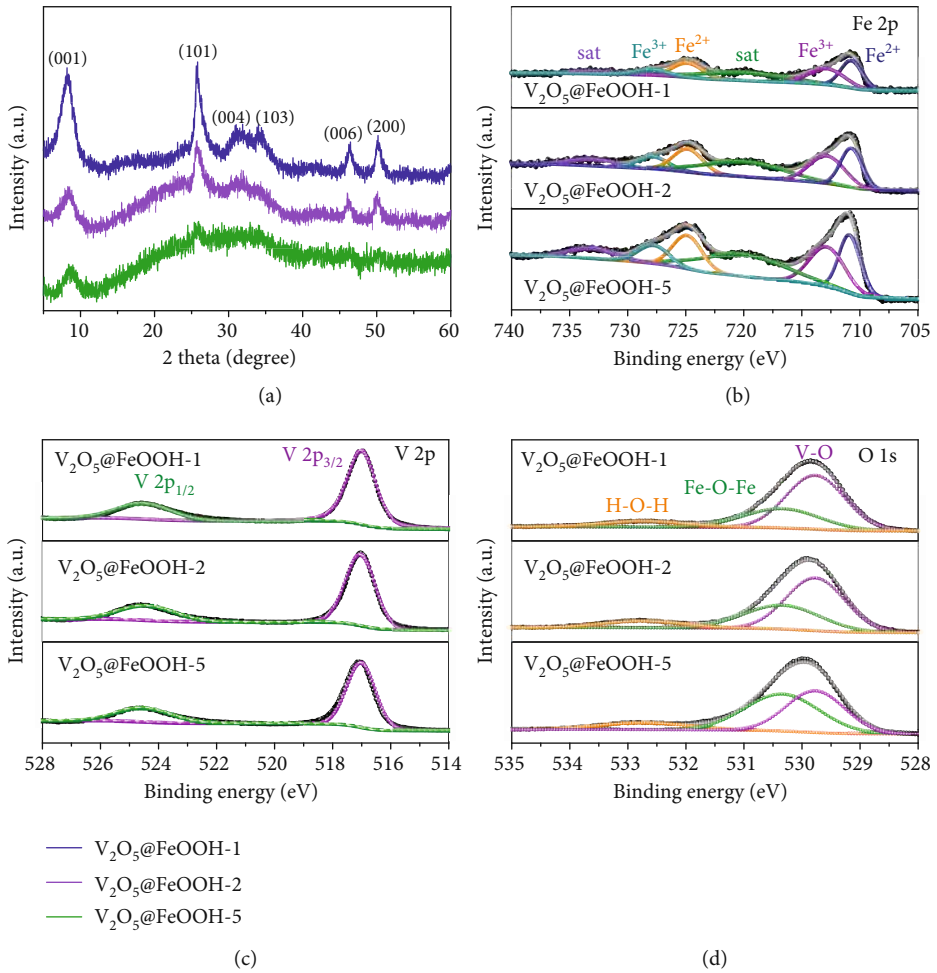

Figure 4: (a) XRD patterns of V_2O_5@FeOOH heterostructures. (b–d) XPS analysis of V_2O_5@FeOOH heterostructures: (b) Fe 2p, (c) V 2p, and (d) O 1s spectra.

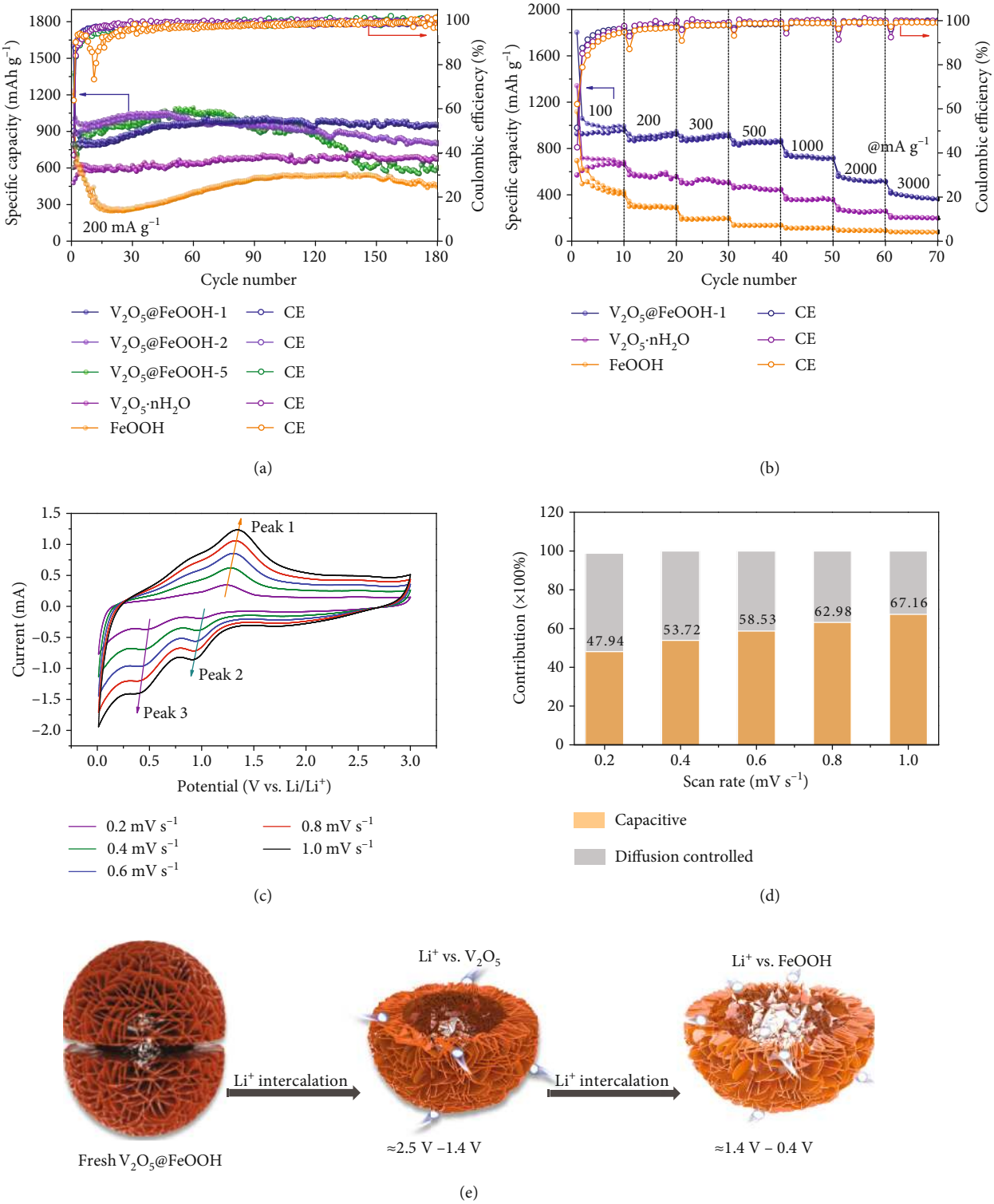

Figure 5: Electrochemical properties in Li^+ storage. (a) Cycling performance of V_2O_5@FeOOH-1, V_2O_5@FeOOH-2, V_2O_5@FeOOH-5, $V_2O_5{\cdot}nH_2O$, and FeOOH at 200 mA g^{-1}. (b) The rate-capacity performance of V_2O_5@FeOOH-1, $V_2O_5{\cdot}nH_2O$, and FeOOH from 100 to 3000 mA g^{-1}. (c) Cyclic voltammetry curves of V_2O_5@FeOOH-1 at a series of scan rates from 0.2 to 1.0 mV s^{-1}. (d) Normalized contribution ratio of capacitive (orange) and diffusion-controlled (gray) capacities at various scan rates. (e) Schematic illustration for V_2O_5@FeOOH-1 electrode during Li^+ intercalation process.

a higher voltage (2.5-1.4 V) [47], during which the volumetric expansion can be effectively restrained owing to the presence of amorphous FeOOH as surface buffers. Afterwards, FeOOH further contributes considerable capacity at lower voltages (1.4-0.4 V) [48], which is also confined within the inner space provided by interconnected nanosheets. Apart from the strain self-reconstruction enabled by the synergy between V_2O_5 and FeOOH, the hollow configuration is highly appealing for strain accommodation and cycling stability during repeated lithiation and delithiation. More importantly, extra Li^+ storage sites together with diffusion channels are created where the presence of amorphous FeOOH domains induce abundant grain boundaries of V_2O_5 and substantial interfacial area, contributing to boosted reaction activity and enhanced Li-storage capacity.

3. Conclusions

In summary, a novel hollow V_2O_5@FeOOH heterostructured nanoflower has been stereoassembled via an efficient and mild method. These nanoflowers composed of well-connected ultrathin nanosheets demonstrate superior advantages including enlarged electrode-electrolyte contact, facilitated charge transfer, and accelerated mass diffusion for LIBs. Owing to the multiple lithiation voltage plateau and well-defined heterointerfaces, the hollow V_2O_5@FeOOH nanoflowers deliver excellent lithium storage properties with a high reversible capacity (985 mAh g^{-1} at 200 mA g^{-1} after 180 cycles) and remarkable cycling stability (95% capacity retention at 2000 mA g^{-1} after 300 cycles). It is expected that the present result can be further extended to optimize other TMO-based materials and shed lights on the development of future energy applications.

4. Material and Methods

4.1. Preparation of V_2O_5@FeOOH Hollow Heterostructures. 0.364 g commercial V_2O_5 powder was mixed with 25 mL DI water and 5 mL H_2O_2 (30 wt%) under stirring for 2 h to form a dark-red solution at room temperature. $Fe(NO_3)_3{\cdot}9H_2O$ was then added to the above mixture under stirring, accompanied with water bath at 50°C overnight. The reddish-brown precipitates were collected by centrifugation and washed with water and ethanol several times. Finally, V_2O_5@FeOOH was obtained by a freeze-drying process. By varying the amount of $Fe(NO_3)_3{\cdot}9H_2O$, a series of V_2O_5@FeOOH heterostructures were prepared and denoted as V_2O_5@FeOOH-1, V_2O_5@FeOOH-2, and V_2O_5@FeOOH-5. Take V_2O_5@FeOOH-2 as an example, the mass ratio of $Fe(NO_3)_3{\cdot}9H_2O$ to V_2O_5 is 2 : 1.

4.2. Preparation of $V_2O_5{\cdot}nH_2O$. 0.364 g commercial V_2O_5 was dispersed in 25 mL DI water under stirring, followed by the addition of 5 mL H_2O_2 (30%) to form a dark-red solution. After aging at room temperature for 2 h, the mixture was maintained at 50°C under stirring overnight to form a hydrogel. Finally, $V_2O_5{\cdot}nH_2O$ was collected after a freeze-drying process.

4.3. Preparation of FeOOH. 0.364 g $Fe(NO_3)_3{\cdot}9H_2O$ was first dissolved in 25 mL DI water containing 5 mL H_2O_2 (30%) under stirring at room temperature. The solution was then maintained at 50°C overnight. The precipitates were rinsed with water and ethanol several times by centrifugation. Finally, the as-obtained product was collected after freeze-drying overnight.

4.4. Materials Characterization. FESEM (JEOL, JSM-7600F) and TEM (JEOL, JEM-2100F) coupled with EDS spectroscopy were used to investigate the morphology, structure and composition of the as-obtained samples. Crystal phases of the obtained samples were identified using XRD (Rigaku, SmartLab with Cu Kα radiation). XPS (Thermo-VG Scientific, ESCALAB 250) was employed to characterize the compositions and valence states of the products.

4.5. Electrochemical Measurements. The electrochemical measurements of the as-prepared active materials were performed according to previously reported procedures [49]. Specifically, CR2032-type coin cells were assembled in an argon-filled glove box with the contents of moisture and oxygen less than 0.5 ppm. 70 wt% of the product (e.g., V_2O_5@FeOOH-1, FeOOH, and $V_2O_5{\cdot}nH_2O$) was mixed with 20 wt% multiwalled carbon nanotube and 10 wt% polyvinylidene difluoride into NMP to prepare the working electrode. The as-obtained slurry was uniformly pasted on the Cu foil with a mass loading of about 1 mg cm^{-2} and dried under vacuum at 60°C for 24 h to remove the solvent. For the LIBs test, the lithium metal foil was used as the counter/reference electrode, 1.0 M $LiPF_6$ dissolved into a mixture of ethylene carbonate (EC), dimethyl carbonate (DMC), and ethyl methyl carbonate (EMC) (EC/DMC/EMC, 1 : 1 : 1, *v*/*v*/*v*) was used as electrolyte, and Celgard 2400 membrane was used as the separator. The galvanostatic charge-discharge tests at various current densities were conducted with a battery testing system (NEWARE, CT-4008) under a voltage range of 0.01 to 3.0 V. The CV curves were obtained on a Bio-logic (VMP-300) electrochemical workstation.

Conflicts of Interest

The authors declare no competing financial interest.

Authors' Contributions

K. Rui, J. X. Zhu, and W. Huang proposed and supervised the project. Y. Zhang carried out most of the experimental work and wrote the original draft of the manuscript. A. M. Huang and K. Hu carried out the morphological characterization. Y. Ding, W. H. Shi, X. H. Cao, and H. J. Lin analysed and discussed the data. All authors discussed the results and commented on the manuscript.

Acknowledgments

This work was financially supported by the National Natural Science Foundation of China (51872139, 51902158, 21706128), the NSF of Jiangsu Province (BK20170045), the Recruitment Program of Global Experts (1211019), the "Six

Talent Peak" Project of Jiangsu Province (XCL-043, XCL-021), and the Natural Science Foundation of Jiangsu Higher Education Institutions (19KJB430002).

Supplementary Materials

Figure S1: SEM images of commercial V_2O_5 powder. Figure S2: SEM images of the vanadium-based intermediate formed immediately after introducing $Fe(NO_3)_3$ at 50°C. Figure S3: SEM images of the vanadium-based intermediate obtained after reacting with $Fe(NO_3)_3$ at 50°C for 3 h. Figure S4: SEM images of the vanadium-based intermediate obtained after reacting with $Fe(NO_3)_3$ at 50°C for 6 h. Figure S5: SEM images of the vanadium-based intermediate obtained after reacting with $Fe(NO_3)_3$ at 50°C for 12 h. Figure S6: The XRD patterns of the vanadium-based intermediate. Figure S7: SEM, TEM images, and corresponding elemental mapping images of pure $V_2O_5{\cdot}nH_2O$. Figure S8: the SAED pattern for V_2O_5@FeOOH-1. Figure S9: SEM, TEM images, and corresponding elemental mapping images of pure FeOOH. Figure S10: Fe 2p XPS spectrum of FeOOH. Figure S11: XPS analysis of pure $V_2O_5{\cdot}nH_2O$. Figure S12: SEM images of V_2O_5@FeOOH-1 after 180 cycles at a current density of 200 mA g^{-1}. Figure S13: cycling performance of V_2O_5@FeOOH-1, $V_2O_5{\cdot}nH_2O$, and FeOOH at a current density of 2000 mA g^{-1}. Figure S14: b value determined by the relationship between scan rate and peak current. Figure S15: plots of $v^{1/2}$ vs. $i/v^{1/2}$ for calculating constants k_1 and k_2 at different potentials. Figure S16: capacitive contribution to charge storage of V_2O_5@FeOOH-1 at 1.0 mV s^{-1}. Figure S17: Nyquist plots of V_2O_5@FeOOH-1, FeOOH, and $V_2O_5{\cdot}nH_2O$. Figure S18: the relationships between $w^{-1/2}$ and Z' in the low-frequency region of V_2O_5@FeOOH-1, FeOOH, and $V_2O_5{\cdot}nH_2O$. Table S1: the molar ratio of V and Fe for V_2O_5@FeOOH-1, V_2O_5@FeOOH-1, and V_2O_5@FeOOH-5 calculated based on XPS results. Table S2: fitted equivalent resistances for EIS results of V_2O_5@FeOOH-1, FeOOH, and $V_2O_5{\cdot}nH_2O$. Table S3: comparison of lithium storage properties of various vanadium-based oxide materials. *(Supplementary Materials)*

References

[1] X. Xu, B. Chen, J. Hu et al., "Heterostructured TiO_2 Spheres with tunable interiors and shells toward improved packing density and pseudocapacitive sodium storage," *Advanced Materials*, vol. 31, no. 46, article 1904589, 2019.

[2] T. Ling, T. Zhang, B. Ge et al., "Well-dispersed nickel- and zinc-tailored electronic structure of a transition metal oxide for highly active alkaline hydrogen evolution reaction," *Advanced Materials*, vol. 31, no. 16, article 1807771, 2019.

[3] Y. Liu, M. Cheng, Z. He et al., "Pothole-rich ultrathin WO_3 nanosheets that trigger N identical with N bond activation of nitrogen for direct nitrate photosynthesis," *Angewandte Chemie International Edition*, vol. 58, no. 3, pp. 731–735, 2019.

[4] Y. Mo, J. Liu, S. Wang et al., "Low-carbon and nanosheathed $ZnCo_2O_4$ Spheroids with porous architecture for boosted lithium storage properties," *Research*, vol. 2019, article 1354829, 11 pages, 2019.

[5] Q. He, X. X. Liu, R. Wu, and J. S. Chen, "PVP-assisted synthesis of self-supported Ni_2P@Carbon for high-performance supercapacitor," *Research*, vol. 2019, article 8013285, 10 pages, 2019.

[6] G. Wang, Y. Yang, D. Han, and Y. Li, "Oxygen defective metal oxides for energy conversion and storage," *Nano Today*, vol. 13, pp. 23–39, 2017.

[7] Y. Lu, L. Yu, and X. W. (. D.). Lou, "Nanostructured conversion-type anode materials for advanced lithium-ion batteries," *Chem*, vol. 4, no. 5, pp. 972–996, 2018.

[8] T. Jiang, F. Bu, X. Feng, I. Shakir, G. Hao, and Y. Xu, "Porous Fe_2O_3 Nanoframeworks encapsulated within three-dimensional graphene as high-performance flexible anode for lithium-ion battery," *ACS Nano*, vol. 11, no. 5, pp. 5140–5147, 2017.

[9] Y. Lu, L. Yu, M. Wu, Y. Wang, and X. W. D. Lou, "Construction of complex Co_3O_4@$Co_3V_2O_8$ Hollow structures from metal-organic frameworks with enhanced lithium storage properties," *Advanced Materials*, vol. 30, no. 1, article 1702875, 2018.

[10] L. Du, H. Lin, Z. Ma et al., "Using and recycling V_2O_5 as high performance anode materials for sustainable lithium ion battery," *Journal of Power Sources*, vol. 424, no. 1, pp. 158–164, 2019.

[11] Y. Xu, Q. Wei, C. Xu et al., "Layer-by-layer $Na_3V_2(PO_4)_3$ Embedded in reduced graphene oxide as superior rate and ultralong-life sodium-ion battery cathode," *Advanced Energy Materials*, vol. 6, no. 14, article 1600389, 2016.

[12] Y. Jiang, X. Zhou, D. Li, X. Cheng, F. Liu, and Y. Yu, "Highly reversible Na storage in $Na_3V_2(PO_4)_3$ by optimizing nanostructure and rational surface engineering," *Advanced Energy Materials*, vol. 8, no. 16, article 1800068, 2018.

[13] L. Shen, S. Chen, J. Maier, and Y. Yu, "Carbon-coated Li_3VO_4 Spheres as constituents of an advanced anode material for high-rate long-life lithium-ion batteries," *Advanced Materials*, vol. 29, no. 33, article 1701571, 2017.

[14] A. Riaz, M. U. Ali, T. G. Enge, T. Tsuzuki, A. Lowe, and W. Lipiński, "Concentration-dependent solar thermochemical CO_2/H_2O splitting performance by vanadia–ceria multiphase metal oxide systems," *Research*, vol. 2020, article 3049534, 12 pages, 2020.

[15] S. Liang, Y. Hu, Z. Nie et al., "Template-free synthesis of ultralarge V_2O_5 nanosheets with exceptional small thickness for high-performance lithium-ion batteries," *Nano Energy*, vol. 13, pp. 58–66, 2015.

[16] C. Wang, L. Zhang, M. Al-Mamun et al., "Lithium Ion Batteries: A hollow-shell structured V_2O_5 Electrode-Based symmetric full Li-ion battery with highest capacity (Adv. Energy Mater. 31/2019)," *Advanced Energy Materials*, vol. 9, no. 31, article 1970120, 2019.

[17] D. Kong, X. Li, Y. Zhang et al., "Encapsulating V_2O_5 into carbon nanotubes enables the synthesis of flexible high-performance lithium ion batteries," *Energy & Environmental Science*, vol. 9, no. 3, pp. 906–911, 2016.

[18] Q. Xu, J. K. Sun, Z. L. Yu et al., "SiO_x Encapsulated in graphene bubble film: an ultrastable Li-ion battery anode," *Advanced Materials*, vol. 30, no. 25, article 1707430, 2018.

[19] J. Hao, J. Zhang, G. Xia et al., "Heterostructure manipulation via in situ localized phase transformation for high-rate and highly durable lithium ion storage," *ACS Nano*, vol. 12, no. 10, pp. 10430–10438, 2018.

[20] Y. Li, Z. Huang, P. K. Kalambate et al., "V_2O_5 nanopaper as a cathode material with high capacity and long cycle life for rechargeable aqueous zinc-ion battery," *Nano Energy*, vol. 60, pp. 752–759, 2019.

[21] G. Chen, L. Yan, H. Luo, and S. Guo, "Nanoscale engineering of heterostructured anode materials for boosting lithium-ion storage," *Advanced Materials*, vol. 28, no. 35, pp. 7580–7602, 2016.

[22] L. Shen, L. Yu, X.-Y. Yu, X. Zhang, and X. W. D. Lou, "Self-templated formation of uniform $NiCo_2O_4$ hollow spheres with complex interior structures for lithium-ion batteries and supercapacitors," *Angewandte Chemie International Edition*, vol. 54, no. 6, pp. 1868–1872, 2015.

[23] M. Du, D. Song, A. Huang et al., "Stereoselectively assembled metal–organic framework (MOF) host for catalytic synthesis of carbon hybrids for alkaline-metal-ion batteries," *Angewandte Chemie International Edition*, vol. 58, no. 16, pp. 5307–5311, 2019.

[24] S. Zhang, Y. Zheng, X. Huang et al., "Structural engineering of hierarchical micro-nanostructured Ge–C framework by controlling the nucleation for ultralong-life Li storage," *Advanced Energy Materials*, vol. 9, no. 19, article 1900081, 2019.

[25] Y. Wang, L. Yu, and X. W. Lou, "Synthesis of highly uniform molybdenum-glycerate spheres and their conversion into hierarchical MoS_2 hollow nanospheres for lithium-ion batteries," *Angewandte Chemie International Edition*, vol. 55, no. 26, pp. 7423–7426, 2016.

[26] J. Zhou, L. Wang, M. Yang et al., "Hierarchical VS_2 Nanosheet assemblies: a universal host material for the reversible storage of alkali metal ions," *Advanced Materials*, vol. 29, no. 35, article 1702061, 2017.

[27] D. Wang, W. Zhou, R. Zhang et al., "MOF-derived Zn-Mn mixed oxides@carbon hollow disks with robust hierarchical structure for high-performance lithium-ion batteries," *Journal of Materials Chemistry A*, vol. 6, no. 7, pp. 2974–2983, 2018.

[28] Z. Ma, K. Rui, Q. Zhang et al., "Self-templated formation of uniform F-CuO hollow octahedra for lithium ion batteries," *Small*, vol. 13, no. 10, article 1603500, 2017.

[29] Y. Zheng, T. Zhou, C. Zhang, J. Mao, H. Liu, and Z. Guo, "Boosted charge transfer in SnS/SnO_2 heterostructures: toward high rate capability for sodium-ion batteries," *Angewandte Chemie International Edition*, vol. 55, no. 10, pp. 3408–3413, 2016.

[30] T. Zhou, W. Lv, J. Li et al., "Twinborn TiO_2-TiN heterostructures enabling smooth trapping-diffusion-conversion of polysulfides towards ultralong life lithium-sulfur batteries," *Energy & Environmental Science*, vol. 10, no. 7, pp. 1694–1703, 2017.

[31] Q. Zhang, Y. Zhou, F. Xu et al., "Topochemical synthesis of 2D carbon hybrids through self-boosting catalytic carbonization of a metal-polymer framework," *Angewandte Chemie International Edition*, vol. 57, no. 50, pp. 16436–16441, 2018.

[32] G. Zhao, K. Rui, S. X. Dou, and W. Sun, "Heterostructures for electrochemical hydrogen evolution reaction: a review," *Advanced Functional Materials*, vol. 28, no. 43, article 1803291, 2018.

[33] Q. Lu, A. L. Wang, Y. Gong et al., "Crystal phase-based epitaxial growth of hybrid noble metal nanostructures on 4H/fcc Au nanowires," *Nature Chemistry*, vol. 10, no. 4, pp. 456–461, 2018.

[34] J. Chen, P. Cui, G. Zhao et al., "Low-coordinate iridium oxide confined on graphitic carbon nitride for highly efficient oxygen evolution," *Angewandte Chemie International Edition*, vol. 58, no. 36, pp. 12540–12544, 2019.

[35] C. Niu, X. Liu, J. Meng et al., "Three dimensional V_2O_5/NaV_6O_{15} hierarchical heterostructures: controlled synthesis and synergistic effect investigated by *in situ* X-ray diffraction," *Nano Energy*, vol. 27, pp. 147–156, 2016.

[36] J. Zhu, L. Cao, Y. Wu et al., "Building 3D structures of vanadium pentoxide nanosheets and application as electrodes in supercapacitors," *Nano Letters*, vol. 13, no. 11, pp. 5408–5413, 2013.

[37] J. Liu, M. Zheng, X. Shi, H. Zeng, and H. Xia, "Amorphous FeOOH quantum dots assembled mesoporous film anchored on graphene nanosheets with superior electrochemical performance for supercapacitors," *Advanced Functional Materials*, vol. 26, no. 6, pp. 919–930, 2016.

[38] J. X. Feng, H. Xu, Y. T. Dong, S. H. Ye, Y. X. Tong, and G. R. Li, "FeOOH/Co/FeOOH hybrid nanotube arrays as high-performance electrocatalysts for the oxygen evolution reaction," *Angewandte Chemie International Edition*, vol. 55, no. 11, pp. 3694–3698, 2016.

[39] Y. Zhang, K. Rui, Z. Ma et al., "Cost-effective vertical carbon nanosheets/iron-based composites as efficient electrocatalysts for water splitting reaction," *Chemistry of Materials*, vol. 30, no. 14, pp. 4762–4769, 2018.

[40] H. T. Tan, X. Rui, H. Yu et al., "Aqueous-based chemical route toward ambient preparation of multicomponent core-shell nanotubes," *ACS Nano*, vol. 8, no. 4, pp. 4004–4014, 2014.

[41] P. Hu, T. Zhu, J. Ma et al., "Porous V_2O_5 microspheres: a high-capacity cathode material for aqueous zinc-ion batteries," *Chemical Communications*, vol. 55, no. 58, pp. 8486–8489, 2019.

[42] J.-Q. Huang, X. Guo, X. Lin, Y. Zhu, and B. Zhang, "Hybrid aqueous/organic electrolytes enable the high-performance Zn-ion batteries," *Research*, vol. 2019, article 2635310, pp. 1–10, 2019.

[43] J. X. Feng, S. H. Ye, H. Xu, Y. X. Tong, and G. R. Li, "Design and synthesis of $FeOOH/CeO_2$ heterolayered nanotube electrocatalysts for the oxygen evolution reaction," *Advanced Materials*, vol. 28, no. 23, pp. 4698–4703, 2016.

[44] M. Du, K. Rui, Y. Chang et al., "Carbon necklace incorporated electroactive reservoir constructing flexible papers for advanced lithium-ion batteries," *Small*, vol. 14, no. 2, article 1702770, 2018.

[45] X. Wang, X.-L. Wu, Y.-G. Guo et al., "Synthesis and lithium storage properties of Co_3O_4 nanosheet-assembled multishelled hollow spheres," *Advanced Functional Materials*, vol. 20, no. 10, pp. 1680–1686, 2010.

[46] J. Yang, Z. Ju, Y. Jiang et al., "Enhanced capacity and rate capability of nitrogen/oxygen dual-doped hard carbon in capacitive potassium-ion storage," *Advanced Materials*, vol. 30, no. 4, article 1700104, 2018.

[47] J. Liu, H. Xia, D. Xue, and L. Lu, "Double-shelled nanocapsules of V_2O_5-based composites as high-performance anode and cathode materials for Li ion batteries," *Journal of the American Chemical Society*, vol. 131, no. 34, pp. 12086-12087, 2009.

[48] Y. Song, Y. Cao, J. Wang et al., "Bottom-up approach design, band structure, and lithium storage properties of atomically thin gamma-FeOOH nanosheets," *ACS Applied Materials & Interfaces*, vol. 8, no. 33, pp. 21334–21342, 2016.

[49] Z. Ma, K. Rui, Y. Zhang et al., "Nitrogen boosts defective vanadium oxide from semiconducting to metallic merit," *Small*, vol. 15, no. 22, article 1900583, 2019.